Process Mapping and Anomaly Detection in Laser Wire Directed Energy Deposition Additive Manufacturing using In-situ Imaging and Process-aware Machine Learning

Anis Assad[1,2,6], Benjamin D. Bevans [1], Willem Potter[3], Prahalada Rao[1,7], Denis Cormier[4], Fernando Deschamps[2], Jakob D. Hamilton[3]*, Iris V. Rivero[5]

[1]Grado Department of Industrial and Systems Engineering, Virginia Polytechnical Institute and State University (Virginia Tech), Blacksburg, VA, USA
[2] Department of Industrial and Systems Engineering, Pontifical Catholic University of Parana, Curitiba, PR, Brazil
[3] Department of Industrial and Manufacturing Systems Engineering, Iowa State University, Ames, IA, USA
[4] Department of Industrial and Systems Engineering, Rochester Institute of Tech., Rochester, NY, USA
[5] Department of Industrial and Systems Engineering, University of Florida, Gainesville, FL, USA
[6] Department of Technology and Innovation, University of Southern Denmark, Sønderborg, Denmark
[7] Mechanical Engineering, Virginia Polytechnical Institute and State University (Virginia Tech), Blacksburg, VA, USA

Abstract

This work concerns the laser wire directed energy deposition (LW-DED) additive manufacturing process. The objectives were two-fold: (1) *process mapping* – demarcating the process states as a function of the processing parameters; and (2) *process monitoring* – detecting process anomalies (instabilities) using data acquired from an in-situ meltpool imaging sensor. The LW-DED process enables high-throughput, near-net shape manufacturing. Without rigorous parameter control, however, LW-DED often introduces defects due to stochastic process drifts. To enhance scalability and reliability, it is essential to understand how LW-DED parameters affect processing regimes, and detect deleterious process drifts. Single-track experiments were conducted over 128 combinations of laser power, scanning velocity, and linear mass density. Four process states were observed via high-speed imaging and delineated as stable, dripping, stubbing, and incomplete melting regimes. Physically intuitive meltpool features were used to train simple machine learning models for classifying the process state into one of the four regimes. The approach was benchmarked against computationally intense, black-box deep machine learning models that directly use as-received meltpool images. Using only six intuitive meltpool morphology and intensity signatures, the approach classified the LW-DED process state with statistical fidelity approaching 90% (F1-score) compared to F1-score ~85% for deep learning models.

Keywords: LW-DED process mapping, process stability, meltpool imaging, process-aware machine learning, deep learning.

1 Introduction

1.1 Objectives and Motivation

This work concerns the laser wire directed energy deposition (LW-DED) metal additive manufacturing process [1]. The objectives were two-fold: (1) *process mapping* – demarcating the process state as a function of the processing parameters; and (2) *process monitoring* – detecting process anomalies (instabilities) using data acquired from an in-situ meltpool imaging sensor. A schematic of the LW-DED process is shown in Figure 1(a). In LW-DED, material in the form of metal wire is melted using energy from a laser and deposited layer-upon-layer. The relative movement of the wire, laser beam, and build plate provided by a machine tool or robot enables creation of three-dimensional, geometrically complex, large volume parts [2].

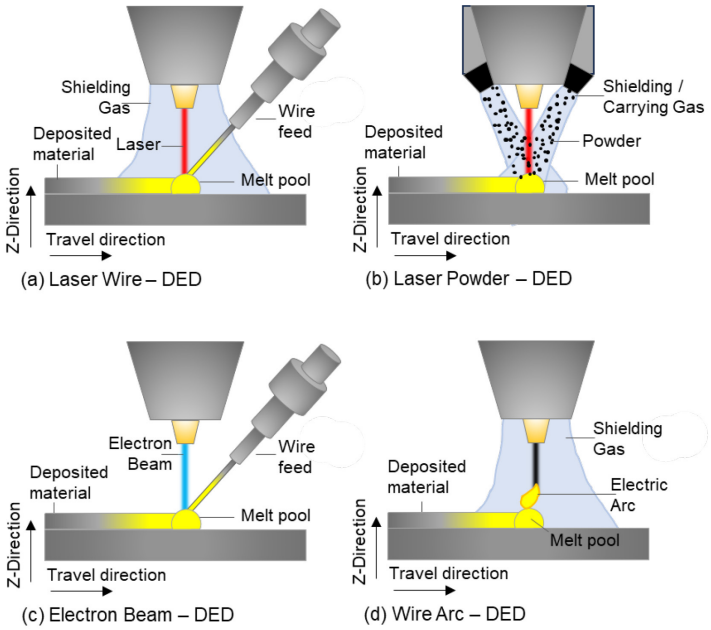

Figure 1: Depiction of various directed energy deposition (DED) additive manufacturing processes. (a) LW-DED (this work); (b) LP-DED; (c) EB-DED; and (d) WA-DED.

The LW-DED process is one of a family of directed energy deposition (DED) additive manufacturing processes [3]. Other DED-based processes include, laser powder directed energy deposition (LP-DED, Figure 1(b)), electron beam wire directed energy deposition (EB-DED Figure 1(c)), and wire arc directed energy deposition (WA-DED, Figure 1(d)) [4]. The salient aspects of these processes are juxtaposed in Table 1. In LP-DED, material is sprayed from a nozzle in powder form and melted using energy from a laser; in EB-DED the feedstock material is metal wire with an electron beam as energy source; and in WA-DED metal wire feedstock is melted using energy from an electric arc akin to gas metal arc welding.

While WA-DED has one of the highest deposition rates of all AM processes, nearly 50 times that of LP-DED, it suffers from relatively poor precision and feature resolution, which necessitates substantial post-process machining and finishing to obtain the final shape [5]. By contrast, LP-DED, whilst relatively precise, has reduced material deposition rates. In this context, LW-DED combines the precision of LP-DED with the large volume deposition capability of WA-DED [6]. Additionally, researchers have reported that not only is the deposition rate of LW-DED an order of magnitude faster than LP-DED, but also that it produces fewer flaws, such as porosity, while maintaining mechanical properties on par with forged components [7, 8]. We note that EB-DED requires a near-vacuum environment to avoid interaction of electrons with other molecules.

Regarding material and mechanical properties, LW-DED also falls in between LP-DED and WA-DED. In all DED processes, there is a significant amount of thermal cycling as molten material is continuously added and solidified layer-upon-layer [9]. Due to the difference in deposition rates, there is a significant difference in the severity of thermal cycling that creates distinctive microstructures and residual stresses [10]. For example, Svetlizky *et. al.* [10] reported that the residual stresses in WA-DED samples significantly exceed the residual stresses of LW-

DED, which in turn had more residual stresses than LP-DED samples. Consequently, given its advantages with respect to deposition rates, resolution, and mechanical properties the LW-DED process is of growing interest for manufacturing large components to near-net shape, such as rocket nose cones, in a rapid and cost-effective manner [10]. Despite these promising capabilities, production-level scale-up of the LW-DED process is currently hindered due to the tendency of the process to drift, despite extensive *a priori* process parameter optimization, resulting in malformed parts [11]. For example, Figure 2 compares turbine blades processed under two similar LW-DED processing conditions. However, the turbine blade in Figure 2 (right) was afflicted by stochastic process instabilities.

Table 1: Comparison of the various types of DED processes [12-14]. The LW-DED process balances the tradeoff between resolution and deposition rate of LP-DED and WA-DED.

	LP-DED	**LW-DED (this work)**	**EW-DED**	**WA-DED**
Feedstock material	Powder	Wire	Wire	Wire
Energy Source	Laser	Laser	Electron Beam	Plasma Arc
Atmosphere	Argon, Nitrogen, etc.	Argon, Nitrogen, etc.	Vacuum	Argon, Nitrogen, ect.
Deposition Rate [kg·hr^{-1}]	2.2	3.0	9.0	10.0
Feature Resolution [mm]	0.25	0.5	0.5	1

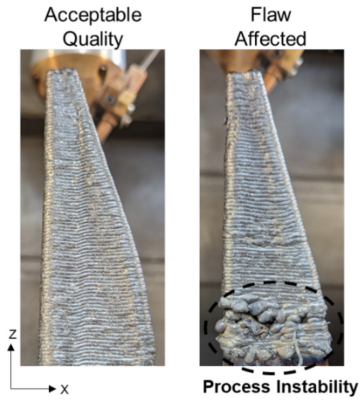

Figure 2: Comparison of an acceptable quality sample and ill-formed production sample of an LW-DED processed turbine blade. Both parts were manufactured under similar conditions.

1.2 Novelty, Approach and Limitations

The novel contributions of this work lie in rigorous mapping of LW-DED process state as a function of key process input variables, and in forwarding an intuitive and computationally tractable process-aware machine learning approach for monitoring the process states. From the process mapping perspective, three common LW-DED process drifts, or instabilities, resulting in sub-optimal deposit geometries are studied in this work, namely, dripping, stubbing, and incomplete melting. Such stochastic process drifts destabilize the complex laser-material interaction inherent to the LW-DED process. The nature and root cause of these drifts are discussed later in the context of Figure 6 in Sec. 3.2. To ensure industrial viability of LW-DED, it is necessary to understand and delineate the processing conditions leading to the onset of process instabilities.

Figure 3 summarizes the approach developed in this work to detect process instabilities. An in-situ high-speed camera is used to acquire images of the meltpool and its surrounding region during LW-DED of stainless steel 316L deposits. Previous works in laser-based additive manufacturing have reported that the morphology (shape) and intensity of the meltpool correlate to process instabilities [15-17]. Accordingly, the meltpool images were analyzed using machine vision algorithms, and a total of six quantitative features (process signatures) pertaining to the meltpool shape and intensity were extracted. These process signatures were used as inputs to various simple machine learning models, such as logistic regression (LR), support vector machine (SVM), k-nearest neighbors (KNN), K-means clustering, and shallow artificial neural networks (ANN). These machine learning models were trained (supervised learning) to classify the LW-DED process state into one of four possible regimes: stable deposition, dripping, stubbing, and incomplete melting. The latter three states are considered unstable processing regimes. The ground

truth for the machine learning algorithm was ascertained by depositing single tracks of stainless steel 316L under 128 combinations of power, velocity, and linear mass density.

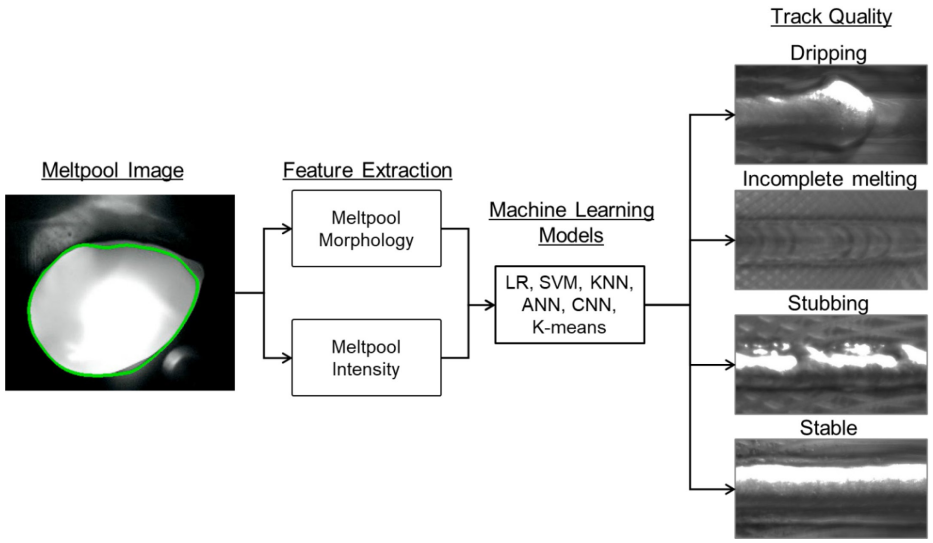

Figure 3: Overview of the approach to correlate in-situ meltpool images to track quality in laser wire DED in the work using meltpool morphology and intensity features.

Lastly, the approach was benchmarked against two deep learning networks that directly use raw meltpool images as opposed to meltpool intensity and morphology features. The two deep learning networks tested were: (i) a custom designed convolutional neural network (CNN), and (ii) a pre-trained CNN called VGG16, which is used in the machine learning community as a benchmark [18]. The approach is termed *process-aware machine learning*, since, physically intuitive features were used as inputs. Deep machine learning architecture, such as convolutional and artificial neural networks, are inherently computationally complex and need to process and store large amounts of raw sensor data [19]. Further, the complexity of deep machine learning models comes at the cost of physical interpretability and transferability [20]. By contrast, the process-aware, machine learning approach, given its computational simplicity, lends itself to real-

time implementation. Moreover, the use of physically intuitive process signatures is amenable to model interpretability and transferability across different processing conditions.

A limitation in the current work is that it is restricted to classification of process states based on data from a single imaging sensor obtained from single track experiments. Since single tracks are the basic building blocks of LW-DED parts, the ability to track and detect instabilities is the first step towards process control in complex parts. Future work will extend the approach to a multi-layer part with heterogeneous sensors for controlling specific functional aspects, such as microstructure evolved and mechanical properties. We will further improve this work beyond process monitoring to in-situ mitigation of process instabilities using a hybrid additive-subtractive correction strategy. The key idea is to use a subtractive machining attachment with the LW-DED system to remove a flaw afflicted layer before they cascade to succeeding layers.

2 Prior work

Whilst several researchers have reported sensor-based monitoring and machine learning for flaw detection in LP-DED and WA-DED, such efforts in the context of LW-DED remain in nascent stages [21]. These prior works in LP-DED and WA-DED focus on prediction of porosity, deformation, and microstructure-related flaws using in-situ sensor data and machine learning [15, 22, 23]. Likewise, researchers have applied in-situ sensing and machine learning for flaw detection in laser welding sans filler wire [24-29]. Rather than meltpool imaging, these works have relied on imaging subsurface weld pools or the laser plume. This is one of the first works to delineate the processing conditions that are liable to cause process instabilities, as well as demonstrate a computationally tractable approach for real-time process monitoring using high-speed meltpool imaging data. Herewith, we review select LW-DED literature in a process mapping, sensing, and monitoring context; a summary of pertinent literature is provided in Table 2.

A major research thrust in LW-DED is toward empirical understanding of process phenomena as a function of processing parameters. For example, Abioye *et al.* [30], conducted an empirical study to ascertain the process regimes in LW-DED. They changed the scan velocity (V) and laser power (P) to determine the region of stable deposition, dripping, stubbing, and incomplete melting. In a similar vein, Ding *et al.* [31] studied the effect of scan path on surface roughness and surface porosity. Other works include understanding the effect of process parameters on solidification microstructure [32]. Motta *et al.* [33] monitored the meltpool with a high-speed camera. They conducted a parameter study to visualize changes in meltpool morphology associated with nominal, dripping, stubbing, and defective processing regimes for a coaxial wire feed LW-DED system. Similarly, Akbari *et al.* [34] monitored the process using a coaxial camera to correlate the meltpool morphology to the microstructure. The present work provides further delineates the relationship between processing parameters and instabilities, through an evolved understanding of the meltpool dynamics.

From a process monitoring and control perspective, Gibson *et al.* [35] and Chen *et al.* [36] used an optical imaging camera installed coaxial to the laser beam to control the meltpool area and width, respectively, via a closed loop controller that modulated the laser power. Abadi *et al.* [37] outline critical considerations in the laser and wire interactions for maintaining stable transfer to the melt pool. These works report that maintaining a stable meltpool morphology resulted in desirable geometric integrity. Sensor-based feedback methods have been key to advancing LW-DED technology. Hagqvist *et al.* [38] showed success in maintaining stable wire feed rates using resistance-based sensing and machine-learning control during the laser-wire DED process. Kisielewicz *et al.* [39] maintained stable liquid metal transfer in hot-wire laser DED using optical vision, spectroscopy, and electrical signals.

Jamnikar *et al.* [40] predicted the track penetration depth, width, and height using a multi-sensor array consisting of two optical cameras, three pyrometers, and an acoustic sensor. The sensor data in the form of raw images from the optical cameras and time series trends from the pyrometers were used as inputs to a convolutional neural network trained to predict the foregoing track quality aspects. Likewise, in a recent work, Abranovic *et al.* [11] installed an optical camera on a robot-based LW-DED apparatus to monitor the meltpool behavior. Subsequently, the authors trained a convolutional deep learning autoencoder to predict the evolution of meltpool behavior for future image frames as a function of prior images. The autoencoder was also leveraged, albeit indirectly, to detect process certain process flaws, namely, dripping, arcing, melt pool oscillation, and wire stubbing. This research differs from the foregoing prior works by Jamnikar *et al.* [40] and Abranovic *et al.* [11] in the following two aspects: (i) the focus of this work is in on mapping as well as detecting process instabilities, as opposed to predicting characteristics, such as solidified meltpool depth and meltpool behavior; and (ii) computationally tractable, process-aware machine learning models with intuitive process signature inputs, such as meltpool intensity and morphology, were trained to classify the process state. By contrast deep learning model directly use the raw meltpool images at the expense of interpretability. Indeed, we demonstrate that the classification fidelity of process-aware machine learning is higher than deep learning.

Dehaghani *et al.* [41] recently demonstrated similar forecasting and closed-loop control using optical images as inputs to an artificial neural network. Understanding and predicting the processing conditions also enables the prediction of the microstructure evolution. Gao *et. al.* [42] found that as the processing regime varied from incomplete melting to stubbing, the cooling rate changed from fast to slow. The varying cooling rate subsequently generated heterogeneous

microstructure. This basic physical understanding is vital for future microstructure control of the LW-DED process.

Table 2: Literature review table for LW-DED in the context of process mapping and monitoring.

Focus	Reference	Sensor	Performed Task
Process Mapping & Understanding	[30]	None	Process mapping
	[31]	None	Scan-path planning
	[32]	None	Microstructure mapping
Correlation of Meltpool Behavior to Processing State	[33]	High-Speed Camera	Visualized meltpool at various regimes
	[34]	Optical Camera	Microstructure correlation with meltpool shape.
Control of Meltpool Behavior	[35]	Optical Camera	Controlled meltpool area to improve geometric accuracy.
	[36]	Optical Camera	Control of meltpool width improved geometric integrity.
Prediction of Part Quality	[40]	High-Speed Camera	Used convolutional neural network to predict track quality
	[11]	Optical Camera	Used convolutional autoencoder to predict meltpool behavior, and process states.

3 Methods

3.1 Experimental setup

A schematic diagram and picture of the experimental setup are shown in Figure 4. A Hybrid Manufacturing Technologies AMBIT FLEX LW-DED system was retrofitted to a Hardinge GX250-5 axis vertical milling center. The milling head with the laser optics controls all travel in the X, Y, and Z axes relative to the substrate. The laser source consisted of an IPG Photonics Yb-doped fiber laser (1070 nm) with maximum power output of 2 kW.

The laser was focused to a nominal 2 mm spot size, and argon gas (flow rate = 20 $L \cdot min^{-1}$) was used for shielding. For in-situ monitoring, an Edgertronic SC2+ high-speed camera was installed off-axis to the laser beam, inclined at a 45º angle and focused on the meltpool. The camera

was affixed to the laser optic system such that it moved in concert with the beam. Thus, a stationary and focused image of the meltpool was obtained throughout the process. The camera captured meltpool images at 2,500 frames per second at a resolution of 1280 × 720 pixels. Approximately 1249 image frames were acquired for each single track at a spatial resolution of 20 µm per pixel.

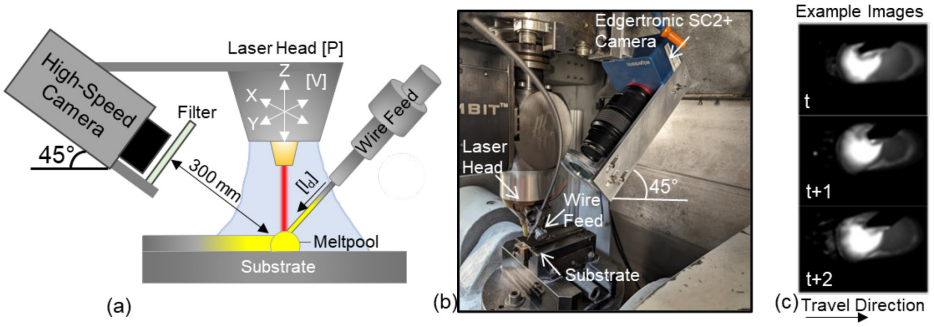

Figure 4: Depiction of the LW-DED apparatus: (a) schematic; (b) image of the apparatus; and (c) exemplar meltpool data.

3.2 Experimental design

Stainless steel 316L wire from Lincoln Electric (diameter 1.1 mm) was used as feedstock for 128 printed single tracks with a length of 40 mm each and an offset height of 11.5 mm. The chemical composition of the wire conformed to ASTM standard A580/A580M [43]. The tracks were deposited parallel to the X-axis with the machine table stationary and the laser head moving. The stainless steel alloy 316L used in this work is an austenitic stainless steel with importance in naval applications due to its corrosion resistance [44-46].

Each single track was produced under distinct process parameters using a full factorial experimental design with three main variables: laser power (P, [W]), scanning velocity (V, [mm·min^{-1}]), and linear mass density (l_d, [g·mm^{-1}]). The scanning velocity refers to the relative speed between the substrate and laser beam. Linear mass density (l_d) is the ratio of the material

feed rate (f_r, [g·s^{-1}]) to the laser scanning velocity (V, [mm·s^{-1}]); $l_d = \frac{f_r}{V}$. An inordinately large l_d value would lead to a large accumulation of material ahead of the meltpool, which is characteristic of stubbing. Insufficient l_d would lead to an incoherent line, as not enough material is available for deposition.

The full factorial experimental design is depicted in Figure 5. The laser power (P) and scanning speed (V), respectively, were evenly spaced at 8-levels ranging between 600 W to 1800 W, and 250 mm·min^{-1} to 1500 mm·min^{-1} respectively. The experimental design was repeated such that two levels of linear mass density were studied: l_d = 0.0086 g·mm^{-1} and l_d = 0.0129 g·mm^{-1}. The laser power and velocity levels were chosen with the intent of engendering various types of process drifts. The linear mass density levels were selected based on manufacturer settings, and with the intent to minimize failure to deposit. The color bar on the right of Figure 5 represents the linear energy density $E_L = \frac{P}{V}[J \cdot mm^{-1}]$.

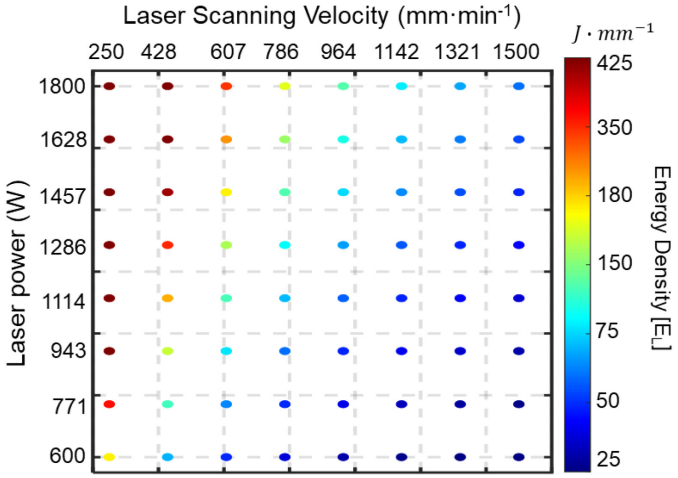

Figure 5: Processing parameters used in the experiment. The color bar to the right is the ratio of laser power to scan velocity (P/V).

Four process regimes were observed during experiments: (a) stable, (b) dripping, (c) stubbing, and (d) incomplete melting. Figure 6 shows representative meltpool images acquired for each regime, and the deposited track. The bottom row of Figure 6 is the cross-section of weld beads representing each regime. The ideal case of stable melting is depicted in Figure 6(a). The dripping regime (Figure 6(b)) is caused by excess energy delivery to the wire which melts the wire before it reaches the meltpool. The surface tension of the melted wire prevents consistent wetting and adherence to the previous layers, and in the case of a single track, fusion of material onto the substrate. Consequently, instead of homogenous connected tracks, dripping results in inconsistent, discontinuous deposits [32, 33].

The stubbing regime of Figure 6(c) results from insufficient energy to melt both the incident wire and previously deposited layers, or the substrate in the case of single-track prints. Consequently, stubs of semi-solid wire protrude from the surface of the meltpool. Incomplete melting in Figure 6(d) is characterized as an extreme case caused either by insufficient energy or insufficient material delivery. The resulting track is characterized by near-complete discontinuity. The meltpool behavior changes dramatically for each of these regimes in terms of its shape (morphology) and its intensity.

Apart from the deposit quality, the width, depth of penetration, and height of the track are also contingent on the processing conditions [16]. Since the focus of this work is on classifying and detecting the process regime, these track quality aspects were not quantified. As evident from Figure 6 (bottom row), under stable processing conditions, the material nominally penetrates the substrate material. In the dripping regime, the material penetrates deeper into the substrate, because the high energy density causes over-melting of the wire and subsequent deposition of material at high temperature. Further, the width of the track in the dripping regime increases as a larger volume

of material is melted. Within the stubbing regime, the lower energy density results in insufficient penetration into the substrate. Under the incomplete melting regime, there is negligible penetration into the substrate, and effectively no material is deposited.

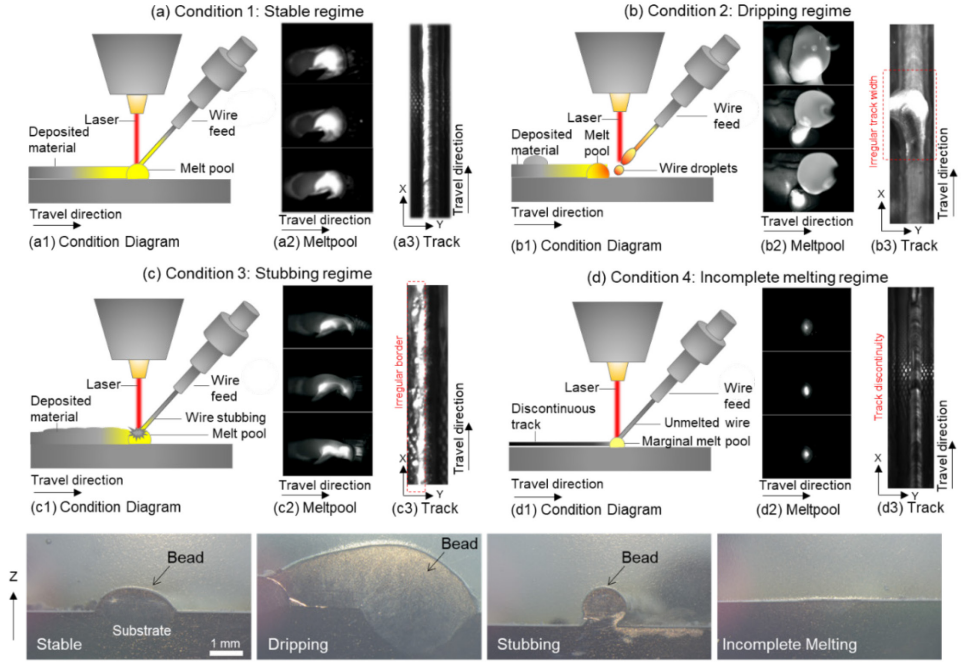

Figure 6: The four processing regimes studied in this work, their meltpool morphologies, and their effect on the quality of the track. (a) stable (b) dripping; (c) stubbing; and (d) incomplete melting.

3.3 Machine Learning

Machine learning algorithms were used to detect (classify) the process regimes from the acquired meltpool. The approach comprises of the following three steps:

- Step 1 - Image pre-processing using computer vision step to detect the meltpool boundary.
- Step 2 - Feature extraction to obtain two types of process signatures from the processed meltpool images, namely meltpool morphology (shapes) and meltpool intensity (brightness). The melt pool intensity is a surrogate for meltpool temperature.
- Step 3 - Training of machine learning models to detect the four process regimes based on the acquired meltpool features.

3.3.1 Image pre-processing

The aim is to separate the meltpool boundary from exogeneous artifacts using well-known computer vision algorithms. The key aspects of this procedure are exemplified in Figure 7. The detection of the meltpool contour was performed by the combination of three computer vision procedures: Gaussian image blurring, binary image thresholding, and image border tracing [47].

While the first two procedures transform the meltpool images to reduce noise from illumination and vibration, the third procedure defines the meltpool contour. All computer vision algorithms were computationally implemented in Python 3.7 with the support of the OpenCV library. Each of the steps are described in detail in Appendix I.

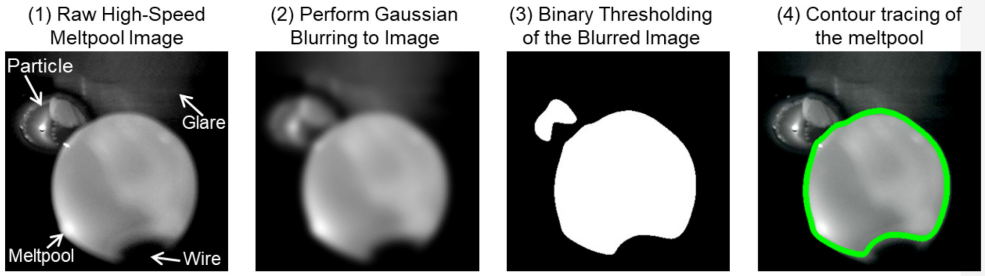

Figure 7: Depiction of the computer vision approach: (1) a grayscale image of the meltpool is captured by the high-speed camera; (2) the image is blurred via a gaussian function; (3) the blurred image is binarized; and (4) the meltpool contour is detected via a border tracing algorithm.

3.3.2 Feature extraction

Two categories of process signatures are extracted from the synthesized meltpool images. These are: (a) meltpool morphology (shape) and (b) meltpool intensity. A total of 6 features were extracted to predict track quality in this work. These six features and their origins are visualized in Figure 8. The choice of meltpool features was motivated from our previously published experimental work in laser-based additive manufacturing processes such as laser powder bed fusion (LPBF) and laser power directed energy deposition (LP-DED), and theoretical simulations by Khairallah and co-workers [16, 17, 48, 49].

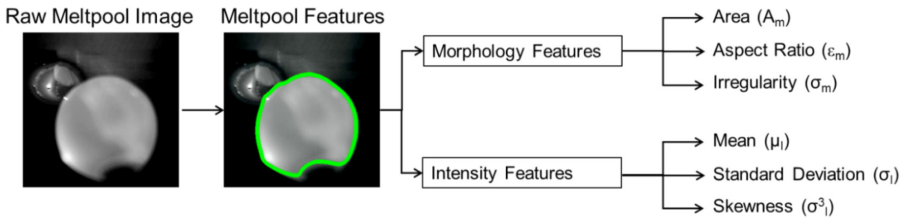

Figure 8: Schematic representative of the source image from which the six used features were extracted.

Described herein are the meltpool morphology and intensity features extracted in this work.

(a) Meltpool morphology features

Morphological features capture the shape of the meltpool as defined by the traced contour. As exemplified in Figure 9, they comprise the meltpool area (A_m), aspect ratio (ε_m), and irregularity (σ_m).

(i) The meltpool area represents the size of the meltpool by summing the number of pixels inside of the traced contour image.

(ii) The meltpool aspect ratio is the length to width ratio of an ellipsoid fitted around the bounded contour of the meltpool. An aspect ratio of $\varepsilon_m = 1$ represents a perfect circle, whereas $\varepsilon_m > 1$ indicates an elongated meltpool.

(iii) The meltpool irregularity is quantified as the standard deviation of all the radii measured from the centroid to each point on the contour borders of the meltpool. As the meltpool contour is traced, it is essentially composed of a sequence of point coordinates that form a closed shape around the meltpool. The meltpool radii are traced from the centroid of the meltpool to every point coordinate along the detected contour. Large meltpool irregularity values indicate ill-shaped meltpools.

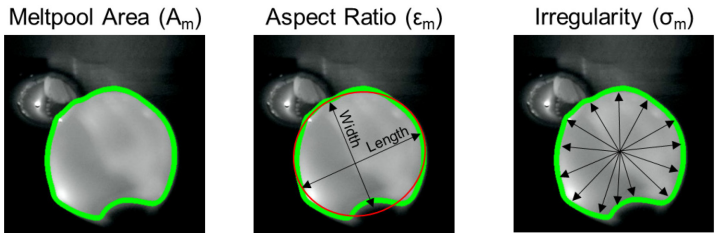

Figure 9: Depiction of the three meltpool morphological features: meltpool area (A_m), aspect ratio (ε_m), and irregularity (σ_m).

(b) Meltpool intensity features

As shown in Figure 10, meltpool intensity features characterize the grayscale value of all the pixels included within the boundary of the traced meltpool contour. The rationale is that the meltpool intensity is proportional to the temperature of the meltpool [50]. The meltpool intensity features comprise the mean meltpool intensity (μ_I), standard deviation of meltpool intensity (σ_I), and skewness of meltpool intensity (σ^3_I). Mean intensity (μ_I) of the meltpool quantifies the average temperature; standard deviation (σ_I) of the meltpool quantifies the temperature distribution; and the skewness (σ^3_I) captures bias in the meltpool temperature.

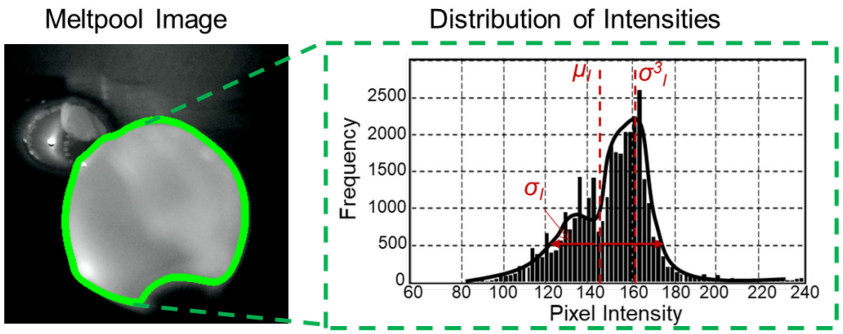

Figure 10: Intensity features within the meltpool contour are plotted as a histogram, the mean (μ_I), standard deviation (σ_I), and skewness (σ^3_I) of the meltpool intensities are quantified.

3.3.3 Model Training and Validation

Supervised machine learning models were used to classify the four process regimes, i.e., dripping, incomplete melting, stubbing, and stable, based on the extracted meltpool features. A depiction of the machine learning pipeline is shown in Figure 11. The classification task was attempted through five simple and easy to implement algorithms, namely: logistic regression (LR), support vector machine (SVM), k-nearest neighbors (KNN), shallow artificial neural networks (ANN), and naïve K-means clustering [16, 17, 40]. The first four of these algorithms are

categorized as supervised learning, while K-means is an unsupervised learning model. Further, two deep learning models, convolutional neural network (CNN) and VGG16 were also tested.

The classification fidelity for each model was assessed in terms of the F1-score. The F1-score metric has been extensively used in classification scenarios in the context of additive manufacturing [17, 49]. The F1-score considers both false positives and false negative rates, thus making it a desirable metric for multi-class classification problem, as shown in Figure 12. The salient aspects of each of the process-aware machine learning models used in this work are summarized in Table 3.

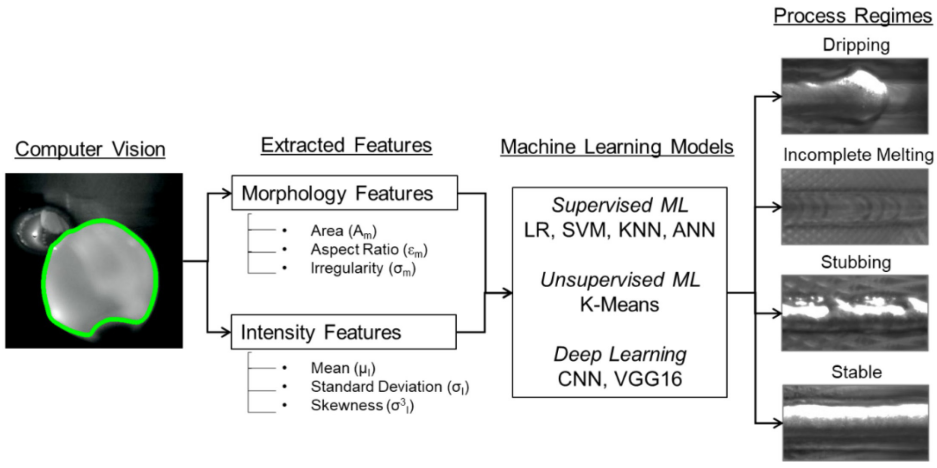

Figure 11: The computer vision-based features are fed as inputs to supervised and unsupervised learning classification algorithms to classify: dripping regime, incomplete melting regime, stubbing regime, or stable regime.

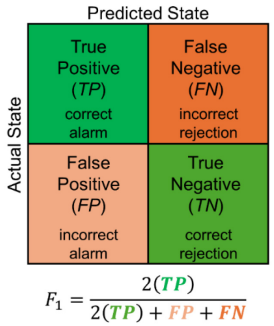

Figure 12: Illustration of the F-1 score metric in the context of a classification task confusion matrix. The F-1 score acts as a harmonic mean that combines precision and recall into a single measurement. Both false positive and false negative misclassifications penalize the metric, providing a balanced estimation of performance.

Table 3: Salient aspects of the five process-aware models investigated in this work.

Model Type	Summary
Logistic Regression	- Linear discriminating equation - L2 regularization penalty - Inverse regularization strength (C): 1 - Tolerance for stopping criterion: 0.00001 - Solver: L-BFGS
Support Vector Machine (SVM)	- Soft margin classifier - Nonlinear kernel: Radial Basis - L2 Regularization - Kernel coefficient (gamma): 0.1 - Inverse regularization strength (C): 1 - Tolerance for stopping criterion: 0.001
K-Nearest Neighbors (KNN)	- Number of neighbors: 101 - Weighting function: uniform weights - Distance metric: Chebyshev - Algorithm: brute-force search
Artificial Neural Network (ANN)	- Number of hidden layers: 1 - Number of neurons: 10 - Activation function: rectified linear unit - L2 Regularization - Solver: stochastic gradient descent (sgd)
K-means	- Number of clusters: 4 - Tolerance for convergence: 0.0001 - Algorithm: Lloyd

Prior to training the machine learning algorithm, the dataset was stratified into training and testing sets as follows. A total of 159,872 images were acquired in this work; 70% of this data was used to train the machine learning algorithms (112,410 images), while 30% of the data was used to test the algorithms (47,462 images). To preclude bias in the machine learning models, all images derived from a specific single track were consistently grouped into either the training or testing dataset. Consequently, the data used for testing the model does not include any data points from single tracks used for model training. The prevention of data leakage across training and testing sets is essential to ensure accurate model evaluation. To tune the hyperparameters of the classification algorithms, an additional 3-fold cross-validation strategy was used within the training dataset (37,470 images per fold).

These process-aware machine learning results were benchmarked against two deep learning convolutional neural networks (CNN) which directly used the meltpool images without intermediate image pre-processing and extraction steps. The first was a CNN architecture specifically designed for this work, and the second CNN was the Visual Graphics Group (VGG16) pre-trained CNN to our decision problem [51]. The VGG16 is widely used as a performance benchmark for custom-designed CNNs, due to its efficiency with image-related classification tasks [20, 52]. To explain further, the VGG16 was pre-trained on the ImageNet dataset (i.e., over 14 million labelled images), and its application to specific problems was operationalized via transfer learning. The CNN and VGG16 models were implemented in Python using the TensorFlow and Keras libraries.

The custom CNN architecture deployed for this work is shown in Figure 13. The input images were resized into 128 × 128-pixel images to reduce the computational complexity of the performed convolutions. In the first convolution layer, 64 kernels of 3 × 3-pixel size were used to produce

distinct feature maps from the same input image. Each kernel traverses the input image and alters its original pixel values according to specific weights learned during the network training process. Subsequently, a pooling layer was used to reduce the spatial complexity of the feature maps by shrinking their size by half in both dimensions. The convolution and pooling steps were then repeated for a second time. Lastly, a dense layer with 256 neurons was used to take the flattened output of the convolution and pooling steps to perform the 4-way classification task, i.e., classification into dripping, incomplete melting, stubbing, or stable regime.

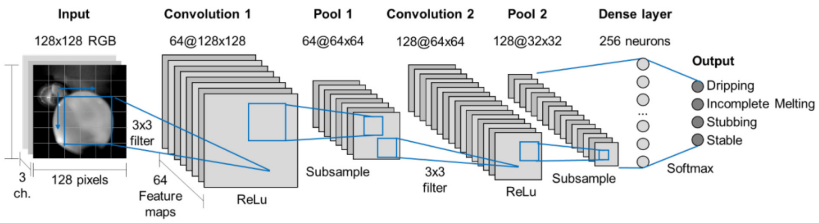

Figure 13: Depiction of the employed convolutional neural network architecture to perform the 4-way classification into dripping, incomplete melting, stubbing, or stable regime.

4 Results

4.1 Effect of processing conditions on process regimes and track morphology

The effect of laser power (P) and scan velocity (V) on the processing regimes is depicted schematically in Figure 14(a) for the representative case of linear material density l_d = 0.0129 g·mm^{-1}. The four regimes, stable, dripping, stubbing and incomplete melting are color-coded. Using a discretized version of the regime map from both levels of linear material densities, a generalized processing map is visualized in Figure 14(b). We note that observing clear demarcations between regimes is a challenging proposition due to inherent stochastic disturbances effecting the process.

As the laser power (P) increases and scan velocity (V) decreases, the resultant energy density ($E_L = P/V$) increases. An inordinate increase in energy density $E_L > 350$ J·mm^{-1} results in excessive melting of the wire leading to dripping. In contrast, as V increases relative to P, E_L decreases, eventually resulting in incomplete melting. Typically, incomplete melting was observed for $E_L <$ 60 J·mm^{-1}. The stubbing regime ($60 < E_L < 150$ J·mm^{-1}) can be considered as an intermediate transition region between stable ($150 < E_L < 350$ J·mm^{-1}) and incomplete melting ($E_L < 60$ J·mm^{-1}).

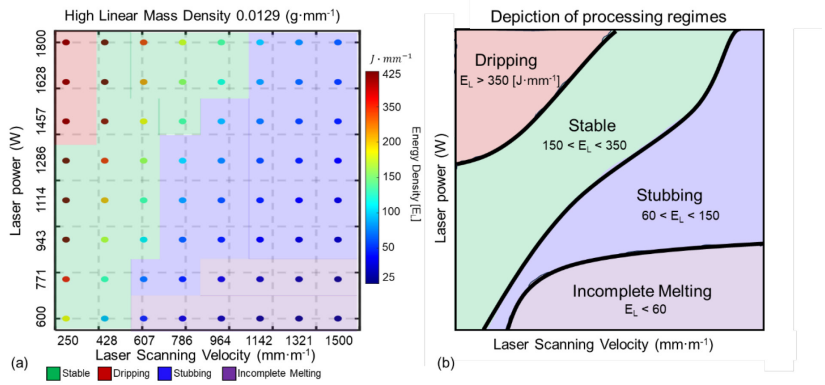

Figure 14: Regime map for the varying laser powers and scan velocities used in this work.

In Figure 15, the track quality is further mapped as a function of laser power (P) and scan velocity (V). In the stable regime, the tracks maintain a consistent width. Then as the input energy increases, the process transitions to the dripping regime in which the line width increases. This is in contrast with the incomplete melting regime which occurs at very low input energy levels in which there is often no material deposition at all due to insufficient energy for melting the wire. Finally, the stubbing regime occurs between the incomplete melting and stable regimes. It is characterized by irregular and rough track boundaries where the wire penetrated the meltpool during deposition. In confirmation of the validity of the process map summarized in Figure 14 and

Figure 15, seven thin-wall parts, as shown in Figure 16, were successfully deposited under stable process regime of 1500 W and 500 mm·min^{-1}, i.e., E_L = 180 J·mm^{-1}. These thin walls measured 150 mm × 2 mm × 10 mm, consisting of 8 layers.

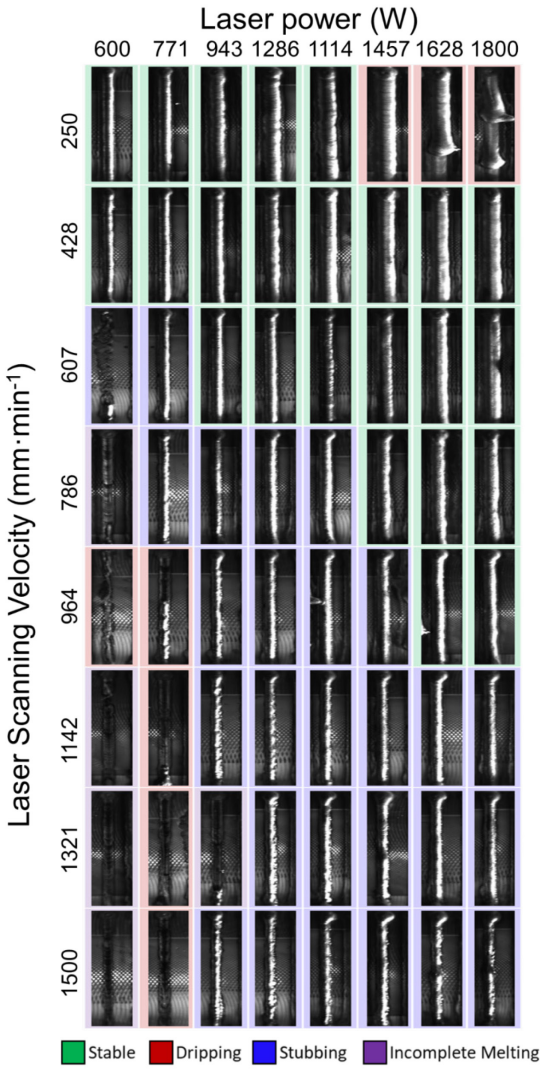

Figure 15: Effect of processing conditions on the LW-DED track quality.

Figure 16: Seven thin-wall parts (150 mm × 2 mm × 10 mm) consisting of 10 layers deposited with processing parameters corresponding to the stable regime (P = 1500 W, V = 500 mm·min^{-1}; E_L = 180 J·mm^{-1}). All seven parts were completed successfully.

4.2 Effect of processing conditions on meltpool characteristics

4.2.1 Qualitative observations

The effect of laser power (P) and scanning velocity (V) on the meltpool characteristics is shown in Figure 17 for linear mass density l_d = 0.0129 g·mm^{-1}. Representative meltpool images for each of the four regimes are presented in Figure 18. Four frames are shown for each regime, and the change in shape and intensity features of the meltpool averaged over the four images for each regime are also reported. A prominent change in the meltpool morphology and intensity between regimes is visually apparent for the four regimes.

The meltpool behavior, shown in Figure 17 and Figure 18, is consistent with the physical track conditions discussed in the context of Figure 15. The apparent size of the meltpool is proportional to the energy density. When E_L > 350 J·mm^{-1}, the realm of the dripping regime has a larger

meltpool area. The meltpool area becomes progressively smaller as the process transitions from stable to stubbing regimes. The area drops to near zero in the incomplete melting regime. Additionally, it is evident from observation that meltpool intensity (μ_I) is proportional to the energy density. Two types of features: (*i*) meltpool morphology and (*ii*) meltpool intensity pattern are plotted as functions of the process regimes in Figure 16.

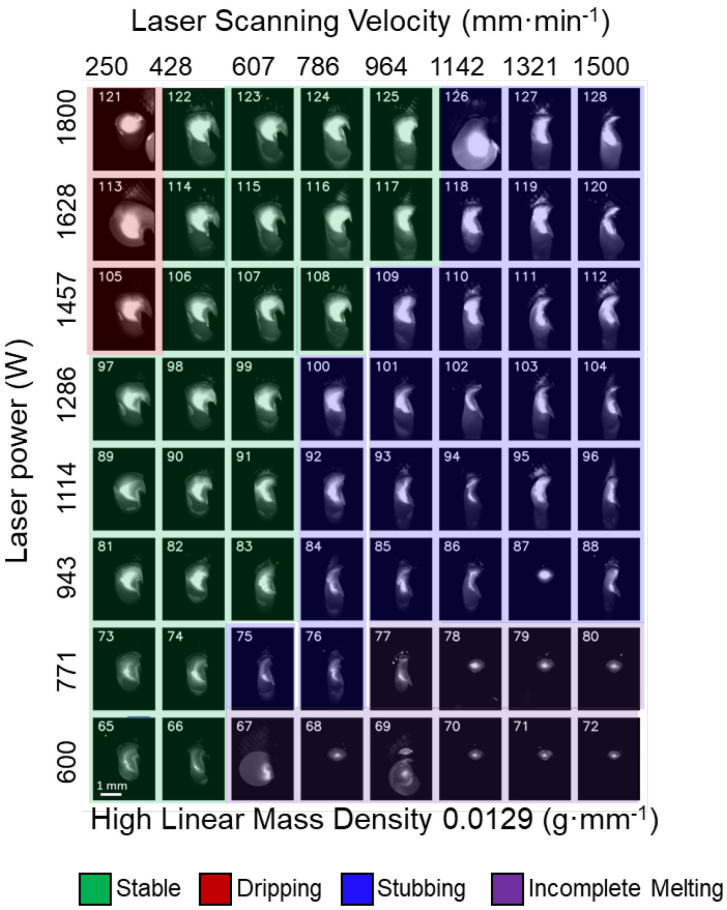

Figure 17: The effect of processing conditions on the meltpool behaviors. These representative meltpools are segmented into the four regimes based on visual observation.

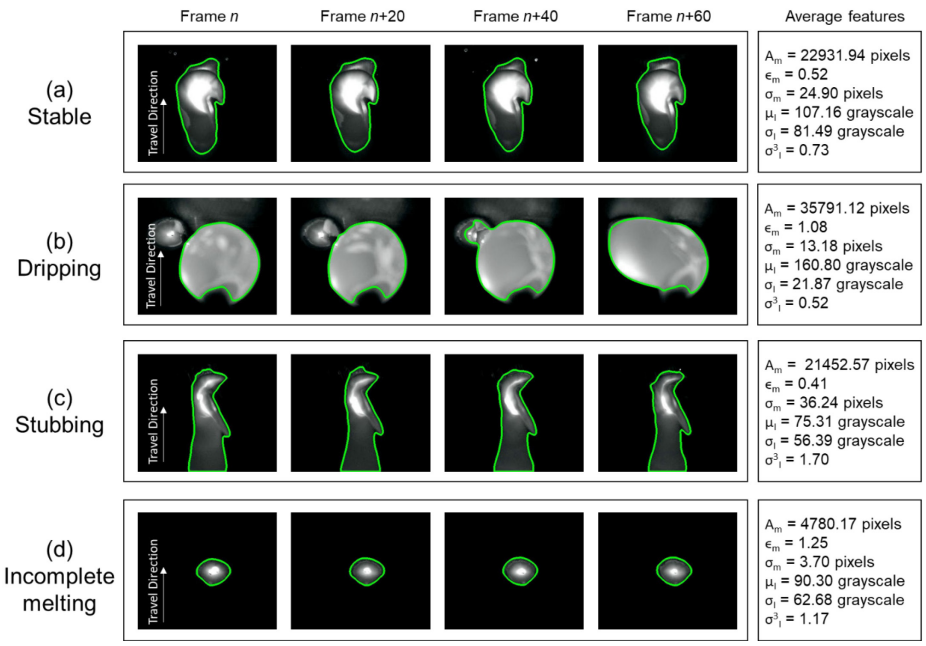

Figure 18: Four consecutive meltpools acquired for each regime. The quantified meltpool morphology and intensity features are shown for the four frames.

4.2.2 Effect on Meltpool Morphology

In Figure 19(a), the mean and ± 1 standard deviation meltpool area (A_m) are plotted for the four regimes. The data is representative of all 159,872 images acquired, of which 61,201 comprise stable, 46,213 dripping, 37,070 stubbing, and 15,388 incomplete melting. Consistent with the qualitative observations discussed in the context of Figure 17 and Figure 18, the average meltpool area increases in proportion to E_L. The average meltpool area is highest for the dripping regime, and smallest in the case of incomplete melting. Indeed, statistical analysis revealed that the average meltpool area is one of the most prominent distinguishing facets across the four regimes. However, the difference between the meltpool area for the stable and stubbing regimes is statistically

indistinguishable, which would hinder clear differentiation between the two process states. This is consistent with the stubbing regime being intermediate to incomplete and stable melting regimes.

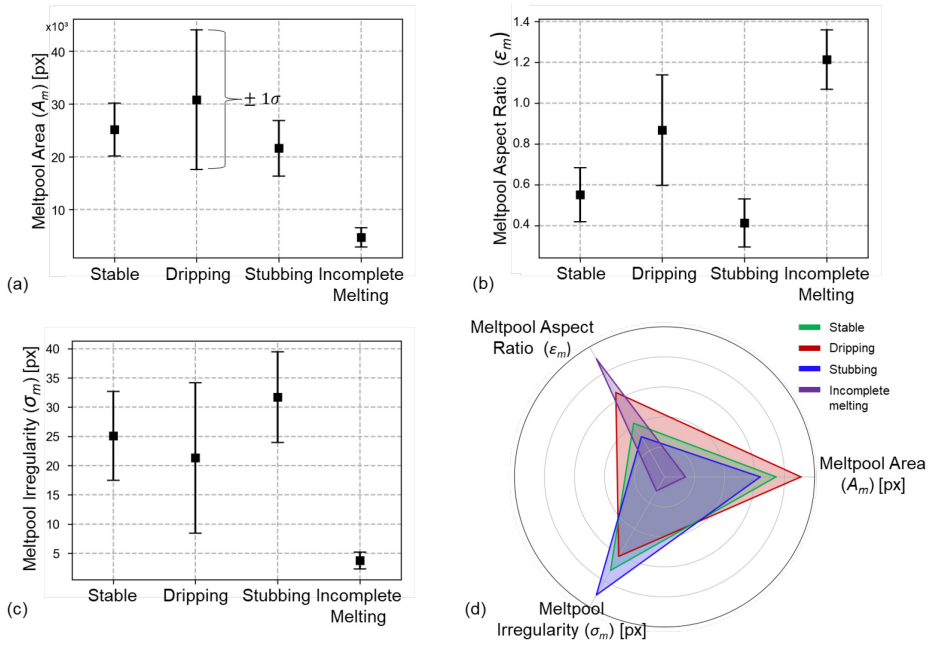

Figure 19: Meltpool morphology features for the four process regimes. (a) meltpool area (A_m), (b) meltpool aspect ratio (ε_m), (c) meltpool irregularity (σ_m), and (d) radar plot of each feature with respect to the process regime.

In Figure 19(b), the meltpool aspect ratio (ε_m), is a prominent discriminator between two groups of regimes: (i) dripping and incomplete melting, and (ii) stable and stubbing. The latter group exhibits elliptical meltpools that are elongated. Dripping and incomplete meltpools, on the other hand, exhibit more circular contours but do not form coherent deposits. However, as in the case with meltpool area, there is significant overlap in the meltpool aspect ratio between the stubbing and stable state.

In Figure 19(c), the meltpool irregularity (σ_m), mirrors the behavior observed for the aspect ratio (ε_m). It is a prominent differentiator of the incomplete melting regime, which has a consistently lower level of irregularity when compared to all other regimes. Further, the meltpool irregularity is a potential differentiator between the stable and stubbing regimes. The average meltpool irregularity is particularly pronounced in the stubbing regime compared to the stable regime.

Continuing with the analysis, the interactions amongst the three meltpool morphology features are presented in Figure 20. The scatter plot depicts a clear separation of dripping and the incomplete melting regimes. Further discrimination is also evident between stubbing and incomplete melting. However, there is a significant overlap in the meltpool morphology features between the stubbing and stable process regimes. This complex nonlinear manifold space necessitates the use of machine learning for classification of LW-DED process regimes.

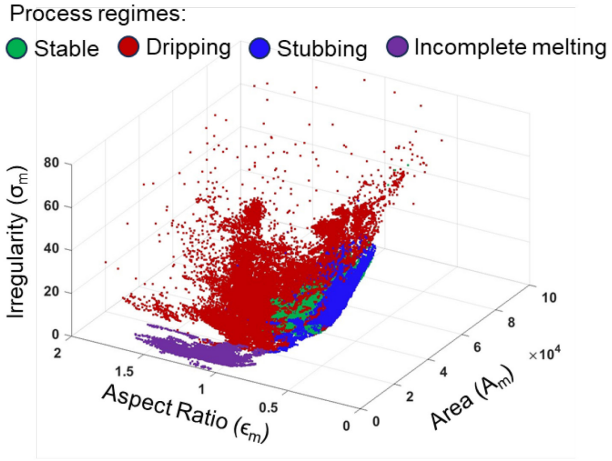

Figure 20: Interactions among the meltpool morphology features for distinct process regimes. meltpool area, meltpool aspect ratio, and meltpool irregularity.

4.2.3 *Effect on Meltpool Intensity*

The three meltpool intensity features as a function of the four process regimes are presented in Figure 21. The average meltpool intensity (μ_I) is proportional to the energy density (E_L). Consequently, the highest meltpool intensity is observed for the dripping regime, and the lowest values for the stubbing and incomplete melting regimes.

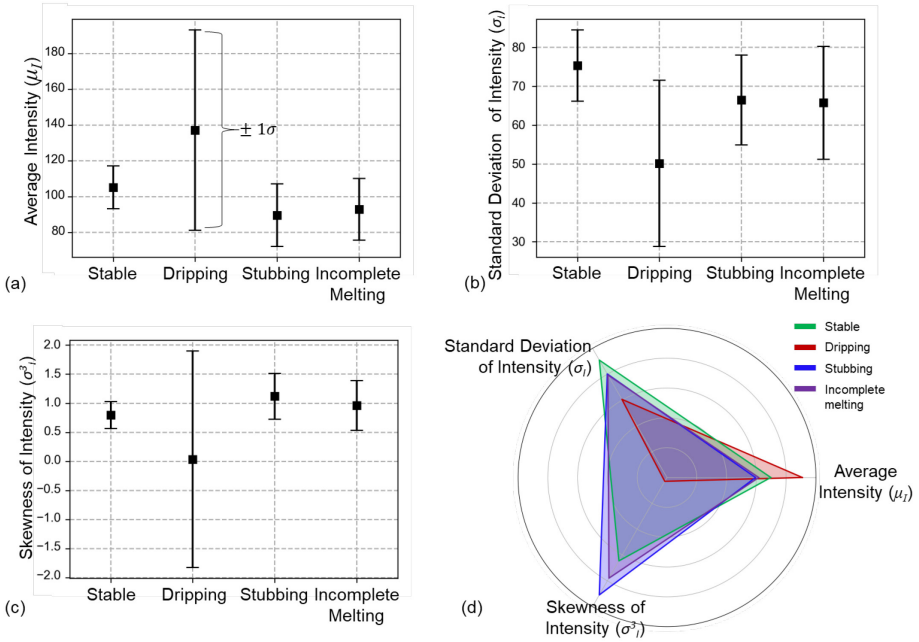

Figure 21: Meltpool intensity features under distinct process regimes. Mean and standard deviation of each feature is plotted for every process (a) for the meltpool average intensity (μI), (b) standard deviation (σI), (c) skewness (σ^3_I), and (d) Radar plot of each feature with respect to the process regime.

The meltpool intensity standard deviation (σ_I) and skewness (σ^3_I) are particularly valuable for differentiating between stable and stubbing regimes. For example, the skewness of the meltpool intensity in the stubbing regime is greater than the stable deposition condition indicating an asymmetrical temperature distribution. Shown in Figure 22 is the interaction among the three meltpool intensity features for the four process regimes. As in the case of the morphological features, while the dripping regime is readily demarcated, there is significant overlap in the other three regimes, which necessitates the use of machine learning classification in separate regimes.

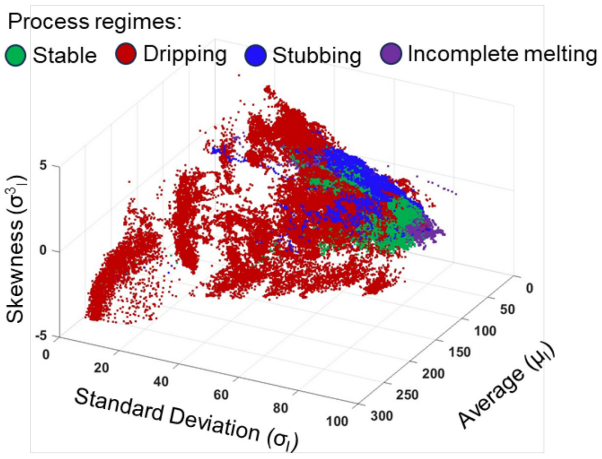

Figure 22: Interactions among the meltpool intensity features for distinct process regimes. Where the dripping regime has a distinctive separation, the other regimes overlap considerably.

4.3 Detection and Classification of Process States with Machine Learning

The classification of LW-DED process regimes is achieved by using the three meltpool morphology and three intensity features as inputs to regression-based supervised learning algorithms, two clustering-based supervised learning algorithms, and one unsupervised learning algorithm. Meltpool morphology and intensity features are labelled as A and B respectively. The F1-score of the classification task is presented in Table 4 for each of the four process-aware

machine learning algorithms, as well as the deep learning algorithms. These reported results were obtained when the models were deployed on the testing dataset alone, ensuring their evaluation reflects generalization towards unseen data.

Further, in Table 4, we compare the results when the morphology (A) and intensity (B) features were used separately and together as inputs to the four simple machine learning models. The results indicate that the morphology-based features alone are capable of distinguishing between the process states with an 87% fidelity (F1-score), compared to 70% using intensity features alone. Combining both types of features, the prediction fidelity increases to 90%. The meltpool images were used directly as input to the two deep learning models in the form of CNN and VGG16. The deep learning models achieved an F1-score of 87%. This result exemplifies the effectiveness of using pragmatic process-aware features and simple machine learning models for process monitoring in LW-DED.

Continuing with the analysis, Table 5 shows the confusion matrix obtained from the SVM model. The confusion matrix encompasses a total of 47,462 data points. The main diagonal of the confusion matrix represents true classifications, while the off-diagonal entries denote misclassifications. The greatest number of misclassifications occur between stable and stubbing regimes. For instance, nearly 1980 data points belonging to the stable regime were misclassified as belonging to stubbing, and 1612 data points from the stubbing regime are incorrectly classified as belonging to the stable regime. The reason for this misclassification is explained in the context of Figure 17, the meltpool dynamics at the periphery of the stubbing regime is similar to that of the stable regime. Further, referring to Figure 20 and Figure 21, a large overlap was observed in the features between the stable and stubbing regimes. Consequently, the limited ability to separate

the stable and stubbing regimes stymies the classification fidelity of machine learning models, including the two deep learning models.

To further evaluate the behavior of process-aware machine learning models, Figure 23 charts the probability of each classification regime using the logistic regression model for each of the 38 single-tracks in the testing data set. In Figure 23, green color represents stable deposition, blue represents stubbing, purple represents incomplete melting, and red represents dripping. The vertical axis is the probability of either stubbing or dripping, and the horizontal axis represents the probability between stable and incomplete melting.

From Figure 23, it is evident that the onset of incomplete melting was always predicted correctly, as there is minimal confusion between it and any of the other three regimes. The probability between stable and stubbing deposition follows the influences from the confusion matrix. In the stubbing condition, 2 out of the 8 stubbing single tracks were misclassified as stable, and 1 out of 16 stable deposits was misclassified as stubbing. Similarly, 1 out of 10 deposits classified as dripping belong to the stubbing regime.

Table 4: F1-score Classification performance for all tested machine learning algorithms. Logistic Regression (LR); K-Nearest Neighbors (KNN); Support Vector Machine (SVM); Multi-Layer Perceptron (MLP); Convolutional Neural Network (CNN).

Model Complexity	Regression		Supervised Learning		Unsupervised Learning	Deep Learning	
Models	LR	KNN	**SVM**	MLP	K-Means	CNN	VGG16
Morphology Features (A)	82.2 %	82.5%	**87.0%**	84.2%	53.3%	87.4 %	87.5%
Intensity Features (B)	55.7 %	62.2%	**69.9%**	59.6%	41.5%		
A +B	89.0 %	85.4%	**90.5%**	88.4%	64.8%		

Table 5: *The confusion matrix for process regime classification from the SVM model (F1-score > 90%).*

		Predicted process regime by the SVM model			
Actual process regime		Stable	Dripping	Stubbing	Incomplete melting
	Stable	**17650**	354	1980	0
	Dripping	174	**11875**	417	24
	Stubbing	1612	379	**8001**	0
	Incomplete melting	0	39	0	**4957**

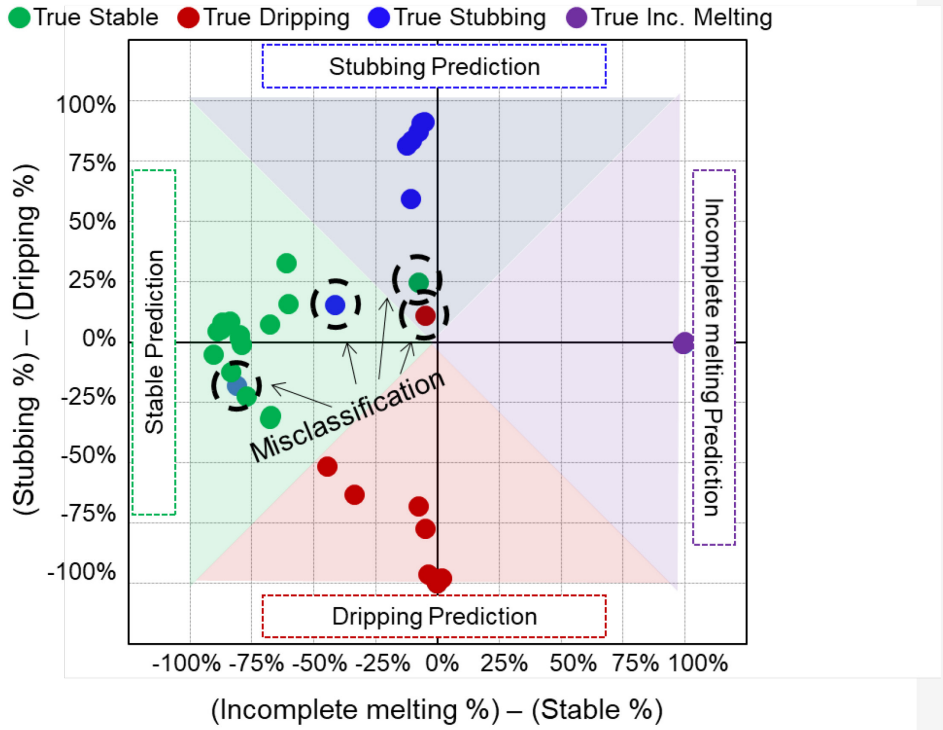

Figure 23: Model decision versus ground truth for each built single track. Model decision comprises the average probability designated for all images accrued for a given single track. The ground truth comprises the quality assessment of the single track.

5 Conclusions

In this work, process instabilities in laser wire directed energy deposition (LW-DED) were detected and classified using meltpool morphology and intensity signatures acquired from an in-situ high-speed imaging camera. The main contribution of this work is in the demarcation of physically intuitive features from meltpool image-based data to distinguish between process states using simple machine learning models. Meltpool morphology and intensity features when used with computationally tractable models, such as the Support Vector Machine (SVM), were as effective in detecting process instabilities as deep learning models, such as convolutional neural networks (CNN), that directly use the meltpool images. Such process-aware machine learning models are amenable for deployment given their computational tractability and interpretability.

Specific conclusions from this work are as follows:

(1) Stainless steel 316L single tracks were deposited under 128 combinations of laser power, velocity, and linear material density conditions to engender different process regimes. The four regimes with respect to the energy density limits are as follows: dripping ($E_L > 350$ J·mm^{-1}); stable ($150 < E_L < 350$ J·mm^{-1}); stubbing ($60 < E_L < 150$ J·mm^{-1}); and incomplete melting ($60 < E_L$ J·mm^{-1}). The feasibility of the stable regime parameters was validated by successfully depositing thin-wall parts.

(2) A high-speed imaging camera focused on the meltpool continuously monitored the process at a sampling rate of 2500 frames per second and resolution of 1280 × 720 pixels. The process was mapped into four regimes: stable deposition, dripping, stubbing, and incomplete melting. The latter three regimes correspond to process instabilities that manifest in sub-optimal parts.

(3) Six physically intuitive features quantifying the meltpool morphology and intensity were extracted from the meltpool images. These six features were motivated from experimental and theoretical simulation results reported in the literature for laser-based additive manufacturing processes. The meltpool signatures were used as inputs to various types of simple machine learning models, such as Logistic Regression (LR), K-Nearest Neighbors (KNN), Support Vector Machine (SVM), shallow artificial neural networks (ANN), and K-means clustering trained to classify the process regime. The regime type was classified with a statistical fidelity (F1-score) exceeding 90% with an SVM using both morphology and intensity features. Morphology features alone resulted in an F1-score of 87%, whilst meltpool intensity features used alone resulted in a lower F1-score of ~70%.

(4) The results obtained from the SVM were comparable to those obtained from two types of deep learning convolutional neural networks - a custom-built network, and the VGG16 model. These deep learning models directly use raw meltpool images instead of meltpool features. The resulting F1-score with the deep learning CCN was ~87%. Thus, process-aware machine learning models using physically intuitive features performed on par with deep learning models.

The use of easy and interpretable physically intuitive process signatures, coupled with process-aware and interpretable machine learning, as opposed to black-box deep learning techniques, facilitates rapid detection of process instabilities and can therefore eliminate the latency in the data transfer and analysis loop inherent to complex data-driven process monitoring algorithms. In effect, this work takes the first step towards future closed loop process control in LW-DED. Our future works will focus on prediction of microstructure evolution and functional properties in practically relevant complex LW-DED parts using heterogeneous sensor data.

Data Availability Statement

The data that support the findings of this study are available from the corresponding author, JDH, upon reasonable request.

References

[1] D. Svetlizky, B. Zheng, A. Vyatskikh, M. Das, S. Bose, A. Bandyopadhyay, J.M. Schoenung, E.J. Lavernia, N. Eliaz, Laser-based directed energy deposition (DED-LB) of advanced materials, Materials Science and Engineering: A 840 (2022) 142967. https://doi.org/10.1016/j.msea.2022.142967

[2] D.-G. Ahn, Directed Energy Deposition (DED) Process: State of the Art, International Journal of Precision Engineering and Manufacturing-Green Technology 8(2) (2021) 703-742. https://doi.org/10.1007/s40684-020-00302-7

[3] T. Özel, H. Shokri, R. Loizeau, A Review on Wire-Fed Directed Energy Deposition Based Metal Additive Manufacturing, Journal of Manufacturing and Materials Processing, 2023. https://doi.org/10.3390/jmmp7010045

[4] S.-H. Li, P. Kumar, S. Chandra, U. Ramamurty, Directed energy deposition of metals: processing, microstructures, and mechanical properties, International Materials Reviews 68(6) (2023) 605-647. https://doi.org/10.1080/09506608.2022.2097411

[5] L.A. Dominguez, F. Xu, A. Shokrani, J.M. Flynn, V. Dhokia, S.T. Newman, Guidelines when considering pre & post processing of large metal additive manufactured parts, Procedia Manufacturing 51 (2020) 684-691. https://doi.org/10.1016/j.promfg.2020.10.096

[6] M.O. Shaikh, C.-C. Chen, H.-C. Chiang, J.-R. Chen, Y.-C. Chou, T.-Y. Kuo, K. Ameyama, C.-H. Chuang, Additive manufacturing using fine wire-based laser metal deposition, Rapid Prototyping Journal 26(3) (2020) 473-483. https://doi.org/10.1108/RPJ-04-2019-0110

[7] Z. Li, S. Sui, X. Ma, H. Tan, C. Zhong, G. Bi, A.T. Clare, A. Gasser, J. Chen, High deposition rate powder- and wire-based laser directed energy deposition of metallic materials: A review, International Journal of Machine Tools and Manufacture 181 (2022) 103942. https://doi.org/10.1016/j.ijmachtools.2022.103942

[8] N. Menon, B.A. Sawyer, C.D. Jamieson, E.W. Reutzel, A. Basak, A Comparison of Microstructure and Microhardness Properties of IN718 Fabricated via Powder- and Wire-Fed Laser-Directed Energy Deposition, Materials, 2023. https://doi.org/10.3390/ma16031129

[9] W.J. Sames, F.A. List, S. Pannala, R.R. Dehoff, S.S. Babu, The metallurgy and processing science of metal additive manufacturing, International Materials Reviews 61(5) (2016) 315-360. https://doi.org/10.1080/09506608.2015.1116649

[10] D. Svetlizky, M. Das, B. Zheng, A.L. Vyatskikh, S. Bose, A. Bandyopadhyay, J.M. Schoenung, E.J. Lavernia, N. Eliaz, Directed energy deposition (DED) additive manufacturing: Physical characteristics, defects, challenges and applications, Materials Today 49 (2021) 271-295. https://doi.org/10.1016/j.mattod.2021.03.020

[11] B. Abranovic, S. Sarkar, E. Chang-Davidson, J. Beuth, Melt pool level flaw detection in laser hot wire directed energy deposition using a convolutional long short-term memory autoencoder, Additive Manufacturing 79 (2024) 103843. https://doi.org/10.1016/j.addma.2023.103843

[12] A. Queguineur, R. Asadi, M. Ostolaza, E.H. Valente, V.K. Nadimpalli, G. Mohanty, J.-Y. Hascoët, I.F. Ituarte, Wire arc additive manufacturing of thin and thick walls made of duplex

stainless steel, The International Journal of Advanced Manufacturing Technology 127(1) (2023) 381-400. https://doi.org/10.1007/s00170-023-11560-5

[13] J. Izdebska-Podsiadły, Chapter 3 - Classification of 3D printing methods, in: J. Izdebska-Podsiadły (Ed.), Polymers for 3D Printing, William Andrew Publishing2022, pp. 23-34. https://doi.org/10.1016/B978-0-12-818311-3.00009-4

[14] H. Siva Prasad, F. Brueckner, A.F.H. Kaplan, Powder incorporation and spatter formation in high deposition rate blown powder directed energy deposition, Additive Manufacturing 35 (2020) 101413. https://doi.org/10.1016/j.addma.2020.101413

[15] M. Khanzadeh, S. Chowdhury, M.A. Tschopp, H.R. Doude, M. Marufuzzaman, L. Bian, In-situ monitoring of melt pool images for porosity prediction in directed energy deposition processes, IISE Transactions 51(5) (2019) 437-455. https://doi.org/10.1080/24725854.2017.1417656

[16] A. Gaikwad, R.J. Williams, H. de Winton, B.D. Bevans, Z. Smoqi, P. Rao, P.A. Hooper, Multi phenomena melt pool sensor data fusion for enhanced process monitoring of laser powder bed fusion additive manufacturing, Materials & Design 221 (2022) 110919. https://doi.org/10.1016/j.matdes.2022.110919

[17] Z. Smoqi, A. Gaikwad, B. Bevans, M.H. Kobir, J. Craig, A. Abul-Haj, A. Peralta, P. Rao, Monitoring and prediction of porosity in laser powder bed fusion using physics-informed meltpool signatures and machine learning, Journal of Materials Processing Technology 304 (2022) 117550. https://doi.org/10.1016/j.jmatprotec.2022.117550

[18] H. Qassim, A. Verma, D. Feinzimer, Compressed residual-VGG16 CNN model for big data places image recognition, 2018 IEEE 8th Annual Computing and Communication Workshop and Conference (CCWC), 2018, pp. 169-175. 10.1109/CCWC.2018.8301729

[19] J. Yang, S. Li, Z. Wang, H. Dong, J. Wang, S. Tang, Using Deep Learning to Detect Defects in Manufacturing: A Comprehensive Survey and Current Challenges, Materials, 2020. https://doi.org/10.3390/ma13245755

[20] Y. Tang, M. Rahmani Dehaghani, G.G. Wang, Review of transfer learning in modeling additive manufacturing processes, Additive Manufacturing 61 (2023) 103357. https://doi.org/10.1016/j.addma.2022.103357

[21] Y. Fu, A.R.J. Downey, L. Yuan, T. Zhang, A. Pratt, Y. Balogun, Machine learning algorithms for defect detection in metal laser-based additive manufacturing: A review, Journal of Manufacturing Processes 75 (2022) 693-710. https://doi.org/10.1016/j.jmapro.2021.12.061

[22] Z.-j. Tang, W.-w. Liu, Y.-w. Wang, K.M. Saleheen, Z.-c. Liu, S.-t. Peng, Z. Zhang, H.-c. Zhang, A review on in situ monitoring technology for directed energy deposition of metals, The International Journal of Advanced Manufacturing Technology 108(11) (2020) 3437-3463. https://doi.org/10.1007/s00170-020-05569-3

[23] Z. Sun, W. Guo, L. Li, In-process measurement of melt pool cross-sectional geometry and grain orientation in a laser directed energy deposition additive manufacturing process, Optics & Laser Technology 129 (2020) 106280. https://doi.org/10.1016/j.optlastec.2020.106280

[24] J. Chen, T. Wang, X. Gao, L. Wei, Real-time monitoring of high-power disk laser welding based on support vector machine, Computers in Industry 94 (2018) 75-81. https://doi.org/10.1016/j.compind.2017.10.003

[25] X.a. Fan, X. Gao, G. Liu, N. Ma, Y. Zhang, Research and prospect of welding monitoring technology based on machine vision, The International Journal of Advanced Manufacturing Technology 115 (2021) 3365-3391. https://doi.org/10.1007/s00170-021-07398-4

[26] T. Lei, Y. Rong, J. Xu, Y. Huang, Experiment study and regression analysis of molten pool in laser welding, Optics & Laser Technology 108 (2018) 534-541. https://doi.org/10.1016/j.optlastec.2018.07.053

[27] Z. Lei, J. Shen, Q. Wang, Y. Chen, Real-time weld geometry prediction based on multi-information using neural network optimized by PCA and GA during thin-plate laser welding, Journal of manufacturing processes 43 (2019) 207-217. https://doi.org/10.1016/j.jmapro.2019.05.013

[28] M. Schweier, M.W. Haubold, M.F. Zaeh, Analysis of spatters in laser welding with beam oscillation: A machine vision approach, CIRP Journal of Manufacturing Science and Technology 14 (2016) 35-42. https://doi.org/10.1016/j.cirpj.2016.05.004

[29] S.A. Shevchik, T. Le-Quang, F.V. Farahani, N. Faivre, B. Meylan, S. Zanoli, K. Wasmer, Laser welding quality monitoring via graph support vector machine with data adaptive kernel, IEEE Access 7 (2019) 93108-93122. https://doi.org/10.1109/ACCESS.2019.2927661

[30] T.E. Abioye, J. Folkes, A.T. Clare, A parametric study of Inconel 625 wire laser deposition, Journal of Materials Processing Technology 213(12) (2013) 2145-2151. https://doi.org/10.1016/j.jmatprotec.2013.06.007

[31] Y. Ding, M. Akbari, R. Kovacevic, Process planning for laser wire-feed metal additive manufacturing system, The International Journal of Advanced Manufacturing Technology 95(1) (2018) 355-365. https://doi.org/10.1007/s00170-017-1179-z

[32] X. Xu, G. Mi, Y. Luo, P. Jiang, X. Shao, C. Wang, Morphologies, microstructures, and mechanical properties of samples produced using laser metal deposition with 316L stainless steel wire, Optics and Lasers in Engineering 94 (2017) 1-11. https://doi.org/10.1016/j.optlaseng.2017.02.008

[33] M. Motta, A.G. Demir, B. Previtali, High-speed imaging and process characterization of coaxial laser metal wire deposition, Additive Manufacturing 22 (2018) 497-507. https://doi.org/10.1016/j.addma.2018.05.043

[34] M. Akbari, R. Kovacevic, An investigation on mechanical and microstructural properties of 316LSi parts fabricated by a robotized laser/wire direct metal deposition system, Additive Manufacturing 23 (2018) 487-497. https://doi.org/10.1016/j.addma.2018.08.031

[35] B.T. Gibson, Y.K. Bandari, B.S. Richardson, W.C. Henry, E.J. Vetland, T.W. Sundermann, L.J. Love, Melt pool size control through multiple closed-loop modalities in laser-wire directed energy deposition of Ti-6Al-4V, Additive Manufacturing 32 (2020) 100993. https://doi.org/10.1016/j.addma.2019.100993

[36] L. Chen, X. Yao, Y. Chew, F. Weng, S.K. Moon, G. Bi, Data-Driven Adaptive Control for Laser-Based Additive Manufacturing with Automatic Controller Tuning, Applied Sciences, 2020. https://doi.org/10.3390/app10227967

[37] S.M.A. Noori Rahim Abadi, Y. Mi, A. Kisielewicz, F. Sikström, I. Choquet, Influence of laser-wire interaction on heat and metal transfer in directed energy deposition, International Journal of Heat and Mass Transfer 205 (2023) 123894. https://doi.org/10.1016/j.ijheatmasstransfer.2023.123894

[38] P. Hagqvist, A. Heralić, A.-K. Christiansson, B. Lennartson, Resistance based iterative learning control of additive manufacturing with wire, Mechatronics 31 (2015) 116-123. https://doi.org/10.1016/j.mechatronics.2015.03.008

[39] A. Kisielewicz, Y. Mi, F. Sikström, A. Ancona, Multi sensor monitoring of the wire-melt pool interaction in hot-wire directed energy deposition using laser beam, IOP Conference Series: Materials Science and Engineering 1296(1) (2023) 012011. https://dx.doi.org/10.1088/1757-899X/1296/1/012011

[40] N.D. Jamnikar, S. Liu, C. Brice, X. Zhang, In-process comprehensive prediction of bead geometry for laser wire-feed DED system using molten pool sensing data and multi-modality CNN, The International Journal of Advanced Manufacturing Technology 121(1) (2022) 903-917. https://doi.org/10.1007/s00170-022-09248-3

[41] M. Rahmani Dehaghani, A. Sahraeidolatkhaneh, M. Nilsen, F. Sikström, P. Sajadi, Y. Tang, G.G. Wang, System identification and closed-loop control of laser hot-wire directed energy deposition using the parameter-signature-quality modeling scheme, Journal of Manufacturing Processes 112 (2024) 1-13. https://doi.org/10.1016/j.jmapro.2024.01.029

[42] L. Gao, A.C. Chuang, P. Kenesei, Z. Ren, L. Balderson, T. Sun, An operando synchrotron study on the effect of wire melting state on solidification microstructures of Inconel 718 in wire-laser directed energy deposition, International Journal of Machine Tools and Manufacture 194 (2024) 104089. https://doi.org/10.1016/j.ijmachtools.2023.104089

[43] A. International, Specification for Stainless Steel Wire, 2023.

[44] R.F. Martins, C.M. Branco, A fatigue and creep study in austenitic stainless steel 316L used in exhaust pipes of naval gas turbines, Fatigue & Fracture of Engineering Materials & Structures 27(9) (2004) 861-871. https://doi.org/10.1111/j.1460-2695.2004.00783.x

[45] S. Gupta, D. Singh, A. Yadav, S. Jain, B. Pratap, A comparative study of 5083 aluminium alloy and 316L stainless steel for shipbuilding material, Materials Today: Proceedings 28 (2020) 2358-2363. https://doi.org/10.1016/j.matpr.2020.04.641

[46] J.M. Korde, A.V. Sreekumar, B. Kandasubramanian, Corrosion inhibition of 316L-type stainless steel under marine environments using epoxy/waste plastic soot coatings, SN Applied Sciences 2(7) (2020) 1267. https://doi.org/10.1007/s42452-020-3096-2

[47] J.M. Blackledge, Chapter 16 - Segmentation and Edge Detection, in: J.M. Blackledge (Ed.), Digital Image Processing, Woodhead Publishing2005, pp. 487-511. https://doi.org/10.1533/9780857099464.4.486

[48] Z. Smoqi, B.D. Bevans, A. Gaikwad, J. Craig, A. Abul-Haj, B. Roeder, B. Macy, J.E. Shield, P. Rao, Closed-loop control of meltpool temperature in directed energy deposition, Materials & Design 215 (2022) 110508. https://doi.org/10.1016/j.matdes.2022.110508

[49] A. Gaikwad, B. Giera, G.M. Guss, J.-B. Forien, M.J. Matthews, P. Rao, Heterogeneous sensing and scientific machine learning for quality assurance in laser powder bed fusion – A single-track study, Additive Manufacturing 36 (2020) 101659. https://doi.org/10.1016/j.addma.2020.101659

[50] P.A. Hooper, Melt pool temperature and cooling rates in laser powder bed fusion, Additive Manufacturing 22 (2018) 548-559. https://doi.org/10.1016/j.addma.2018.05.032

[51] K. Simonyan, A. Zisserman, Very deep convolutional networks for large-scale image recognition, arXiv preprint arXiv:1409.1556 (2014). https://doi.org/10.48550/arXiv.1409.1556

[52] V. Pandiyan, R. Drissi-Daoudi, S. Shevchik, G. Masinelli, T. Le-Quang, R. Logé, K. Wasmer, Deep transfer learning of additive manufacturing mechanisms across materials in metal-based laser powder bed fusion process, Journal of Materials Processing Technology 303 (2022) 117531. https://doi.org/10.1016/j.jmatprotec.2022.117531

[53] E.S. Gedraite, M. Hadad, Investigation on the effect of a Gaussian Blur in image filtering and segmentation, Proceedings ELMAR-2011, 2011, pp. 393-396.

[54] G. Papari, N. Petkov, Edge and line oriented contour detection: State of the art, Image and Vision Computing 29(2) (2011) 79-103. https://doi.org/10.1016/j.imavis.2010.08.009

[55] D. Yang, B. Peng, Z. Al-Huda, A. Malik, D. Zhai, An overview of edge and object contour detection, Neurocomputing 488 (2022) 470-493. https://doi.org/10.1016/j.neucom.2022.02.079

Appendix I

The Gaussian blurring procedure employs a convolution filter with a Gaussian matrix acting as the underlying kernel. It substitutes every pixel in the input image by a weighted combination of its neighboring pixels. Specifically, the neighbor weights are determined according to a Gaussian function [53]. As it allows for every pixel value to become an average blend of nearby pixels, Gaussian blurring reduces the effect of sources of noise that appear as localized fluctuation in pixel values. For this reason, it has become an established preliminary method in contour detection tasks [54].

For this application, the blurring was performed via 31-pixel width and 31-pixel height kernels applied over the input images of 1280-pixel width and 720-pixel height. After the definition of the blurring, a convolution operation was performed between the image and the Gaussian kernel for every pixel position. This operation essentially involves moving the kernel over the image and calculating the weighted sum of the neighboring pixel values, with the weights provided by the Gaussian kernel. Since pixels located on the edges of the image do not have a complete neighborhood for the kernel to operate, missing neighboring pixels are filled with the values of the nearest border pixels.

Following the application of blurring, the next procedure in the computer vision pipeline comprises a binary image thresholding procedure. Binary thresholding is a technique used to highlight regions with distinct color intensity by assigning every pixel grayscale value to either 0 (black) or 255 (white), based on the comparison of its original value against a predefined threshold *T*. If the intensity of a given pixel is greater than or equal to the threshold value, the pixel is assigned a value of 255, while pixels with intensities below the threshold value are assigned a value of 0, effectively converting the image into a binary representation. The value of *T* for this

application is defined by an adaptive thresholding algorithm, detailed subsequently. As it accentuates the borders between image regions with contrasting colors (*e.g.*, the meltpool border), binary thresholding serves as a preliminary step to contour detection [55].

The next computer vision procedure comprises the use of a border tracing approach to detect the contours of the shapes found in the binarized image, and the subsequent definition of the meltpool contour. The tracing of the meltpool contour as a result of these algorithms is visualized in Figure 24. The representative meltpool is from the dripping regime meltpool that requires a high enough threshold parameter to isolate the meltpool area from its surrounding lighting noise. A final image processing procedure was added to ensure adequate contour selection in case multiple contours were detected. This is a common occurrence in the dripping regime. An example of the multiple contour selection procedure can be viewed in Figure 25.

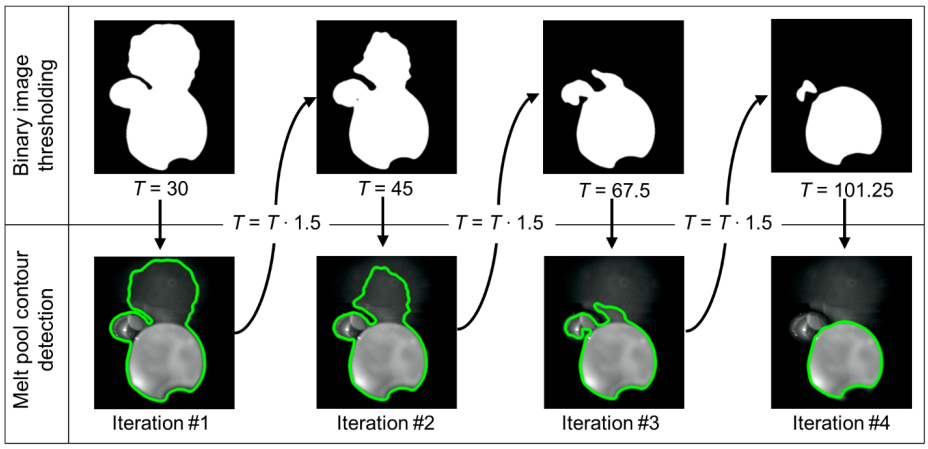

Figure 24: Progressive refinements in contour detection due to the adaptive threshold algorithm. The threshold parameter T is increased, within a predefined limit of iterations, while the contour roundness is improved and no drastic drops in the area metric occur.

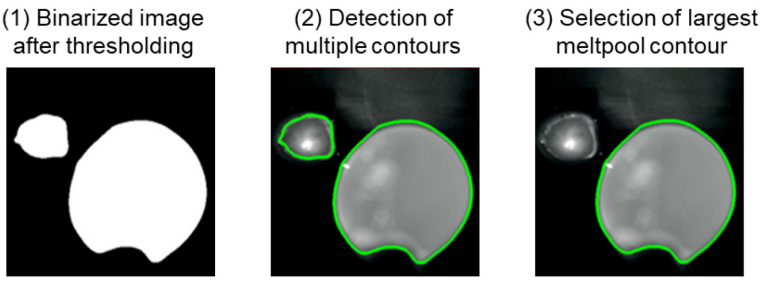

Figure 25: Progressive steps of multiple contour selection: (a) an optimized parameter is achieved for the binary threshold after the execution of the adaptive thresholding algorithm. (b) two contours of significant area are detected after the application of the contour tracing algorithm. (c) the adequate meltpool contour is chosen based on its size and brightness characteristics.

Acknowledgements

Prahalada Rao acknowledges funding from the National Science Foundation (NSF) via Grant numbers: CMMI-2309483/1752069, OIA-1929172, PFI-TT 2322322/2044710, CMMI-1920245, ECCS-2020246, CMMI-1739696, and CMMI-1719388, Department of Energy (DE-SC0021136), Department of Defense, Naval Surface Warfare Center (NAVAIR, N6833524C0215) and National Institute of Standards and Technology (NIST 70NANB23H029T) for funding his research program. Understanding the causal influence of process parameters on part quality and detection of defect formation using in-situ sensing was the major aspect of CMMI-2309483/1752069 (Program Officer: Pranav Soman). The use of machine learning and analytics for process diagnosis in additive manufacturing was funded via ECCS-2020246 (program officer: Richard Nash). Benjamin Bevans was funded through CMMI-2309483/1752069 and PFI-TT 2322322/2044710 Anis Assad and Fernando Deschamps were funded by the Coordenação de Aperfeiçoamento de Pessoal de Nível Superior – Brasil (CAPES) – Finance Code 001. The foregoing also funded a visiting student scholarship for Anis Assad to work at Virginia Tech under the supervision of Prahalada Rao.